Physica C: Superconductivity and its applications 624 (2024) 1354565

Contents lists available at ScienceDirect

Physica C: Superconductivity and its applications

journal homepage: www.elsevier.com/locate/physc

Full length article

Maximizing flux pinning in YBCO coated conductor films for high-field applications

T. Vaimala [a], M.M. Aye [a,b], E. Rivasto [a,c], Y. Zhao [d], H. Huhtinen [a,*], P. Paturi [a]

[a] Wihuri Physical Laboratory, Department of Physics and Astronomy, University of Turku, FI 20014, Turku, Finland
[b] University of Turku Graduate School (UTUGS), University of Turku, FI 20014, Turku, Finland
[c] CP3-Origins, University of Southern Denmark, Campusvej 55, 5230 Odense M, Denmark
[d] School of Electronic Information and Electrical Engineering, Shanghai Jiao Tong University, 200240 Shanghai, People's Republic of China

ARTICLE INFO

Keywords:
High-temperature superconductors
Coated conductors
YBCO
Artificial pinning centers
BZO doping
Nanorod growth
Critical current density
Flux pinning

ABSTRACT

Our study explores the relationship between BZO nanorod density and magnetic flux pinning in YBCO thin films on coated conductor templates. We identified an optimal BZO doping level of 8%–10%, which maximizes flux pinning and enables the highest critical current densities to be achieved across various temperatures and magnetic field ranges, especially in new types of multilayer structures. Additionally, the formation of a *c*-axis peak in the angular-dependent critical current curves at high BZO concentrations underscores the significance of collective pinning mechanisms. These results are discussed using a simple pinning model that considers the effects of nanorod spacing and fragmentation. Overall, our findings contribute to the development of high-performance coated conductor layer structures for future power applications, where maximizing flux pinning is essential.

1. Introduction

High-temperature superconducting (HTS) materials have attracted significant attention due to their potential to revolutionize practical applications such as power generation and transmission, energy storage and microwave applications related to quantum technology [1–5]. Among the HTS materials, thin film and coated conductor technologies have been developed for a wide range of power applications [3,6–11], including HTS magnets for future fusion reactors [12,13]. HTS materials and the technologies based on them are superior and offer several advantages over conventional methods, including high critical current density and low losses, which enable more efficient and compact devices. However, there is still room for improvement and optimization, as the practical applications of HTS materials are limited by weak flux pinning, leading to lower critical current density and limiting the magnetic field they can sustain. Therefore, developing techniques to enhance flux pinning properties has become an important research area [14–22].

To maximize flux pinning and thus the overall critical current density of HTS materials and coated conductors in various temperature and external magnetic field ranges, several approaches have been developed, including intrinsic defects, nanostructured materials, various substrates, multilayer structures, and artificial pinning centers [1,23–25]. One controlled way to enhance flux pinning is to intentionally add various types of defects including nanodots, nanorods, nanoparticles of different materials such as metal, oxides and fluorides [26–30]. Especially, the dopant as $BaZrO_3$ (BZO), which during the pulsed laser deposition forms through the film penetrating nanorods, has been one of the most studied pinning center within the $YBa_2Cu_3O_{6+x}$ (YBCO) lattice [31–33]. However, the effectiveness of BZO doping depends on the concentration, distribution, diameter, length and direction of the nanorods [11,34–37]. Therefore, for ensuring the isotropic improvement of critical current density, the angular dependent studies have been in a crucial role when maximizing J_c for future applications. Recently, a bilayer structure, where optimal crystalline quality producing maximal self-field J_c and, on the other hand, maximal flux pinning structure related to in-field properties are implemented in separate layers, have been of intensive study [25,38–40].

Coated conductors, which offer advantages such as greater flexibility and mechanical strength compared to thin films on single crystal substrates, face many challenges because the substrate can negatively affect the superconducting properties [28,41,42]. Numerous efforts to improve the buffer layer stack on metallic templates have led to compatible lattice structures, epitaxial growth of YBCO, and improved crystal structures of the HTS layer [43,44]. However, challenges remain in reducing thermal stress between the substrate and film, minimizing grain boundary formation, and improving surface roughness of the

* Corresponding author.
E-mail address: hannu.huhtinen@utu.fi (H. Huhtinen).

https://doi.org/10.1016/j.physc.2024.1354565
Received 27 May 2024; Received in revised form 26 June 2024; Accepted 5 July 2024
Available online 22 August 2024

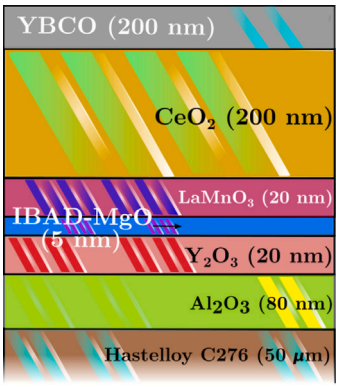

Fig. 1. An advanced buffer layer structure used together with the metallic hastelloy C276. The Gray YBCO layer on the top refers the YBCO doped with BZO nanorods of different concentrations presented in this work.

films. Coordinating all these challenges, especially optimizing the artificial pinning center network in the buffered metal template to achieve maximum flux pinning across various magnetic field ranges, will be one of the biggest goals in the near future.

To promote the use of HTS coated conductors in future applications, we investigated the effect of BZO doping concentration within the YBCO matrix to achieve maximum magnetic flux pinning in thin films deposited on buffered metallic templates. Strain relaxation and the growth of YBCO and BZO nanorods were studied using x-ray diffraction and transmission electron microscopy. These results were connected to the magnetic and transport properties, along with theoretical calculations, to clarify the anisotropy of the critical current and the optimal flux pinning properties in YBCO thin films with different BZO doping levels.

2. Experimental details

A set of superconducting YBCO thin films doped with artificial pinning centers of BZO concentrations 0, 2, 4, 6, 8, 10 and 12 wt.%; hereafter 0BZO, 2BZO, 4BZO, 6BZO, 8BZO, 10BZO and 12BZO, respectively, were deposited by pulsed laser deposition (PLD) on buffered metal hastelloy C276 with an advanced Al_2O_3/Y_2O_3/IBAD-MgO/$LaMnO_3$/CeO_2 buffer layer (Fig. 1) [11]. The details of the growth process together with applied deposition parameters are presented in our previous works [11,45,46].

The crystallographic properties of the films were studied by x-ray diffraction (XRD) using PANalytical Empyrean diffractometer in Bragg–Brentano mode. High-resolution transmission electron microscopy (HRTEM) was performed with a JEOL JEM-2200FS electron microscope combined with a 200 kV field emission gun (FEG) and in-column energy filter (Omega filter). Additionally, a probe-corrected scanning TEM using high-angle annular dark-field imaging (HAADF STEM) was performed with Titan 80–300 at the voltage of 200 kV. The magnetic measurements were implemented using a Quantum Design PPMS system, where the critical current densities were calculated from the openings of the hysteresis loops using the Bean model [47]. The angular dependent critical current densities $J_c(\theta)$ of the films were done at 40 K and magnetic fields up to 8 T by the standard four-probe measurements for 50 μm stripes using horizontal rotation option of PPMS.

The correspondence between the results of the structural and magnetic measurements are quantitatively discussed using a numerical pinning model in accordance with the Ginzburg–Landau theory.

Table 1
Structural properties of the differently BZO-doped YBCO thin films determined by XRD measurements.

Sample	c (Å)	$\Delta\theta$ (°)	$\Delta\phi$ (°)	$\Delta\omega$ (°)	LM (%)	ε_{WH} (%)	$I(005)/I(004)$
0BZO	11.70	0.12	2.12	1.80	0.17	0.15	13.4
2BZO	11.72	0.22	2.37	1.70	0.34	0.31	15.4
4BZO	11.74	0.18	3.66	2.27	0.51	0.25	14.9
6BZO	11.75	0.17	2.71	1.91	0.60	0.30	12.1
8BZO	11.78	0.26	3.49	2.29	0.86	0.37	15.3
10BZO	11.79	0.32	3.41	2.28	0.94	0.35	16.4
12BZO	11.81	0.58	3.90	2.55	1.11	0.27	16.1

3. Results and discussion

3.1. Growth of YBCO lattice and BZO nanorods

The influence on BZO doping on the purity and crystalline quality of YBCO and BZO nanorods were studied by XRD θ-2θ-, ϕ- and ω-scans of the films, and the most critical parameters are collected in Table 1. In the θ-2θ diffractograms (not shown here) only peaks from YBCO, BZO and CeO_2 were obtained, which is a clear indication of sufficient purity although the positions and widths of the peaks change as a function of BZO concentration. Particularly, the (00l) peaks are shifted to lower 2θ values with increasing BZO concentration, indicating significantly lengthened YBCO c-axis and thus increased uniform strain in YBCO lattice. The same effect can also be seen in calculated lattice mismatch values, as shown in Table 1.

When looking at the peak widths (FWHM) in the in-plane and out-of-plane directions, we notice that $\Delta\theta$, $\Delta\phi$ and $\Delta\omega$ all increase remarkably with increasing BZO concentration. Especially, the nonuniform strain along the ab-plane of YBCO is clearly increased, since the peaks in 2θ direction are drastically broadened with BZO concentrations above 6%. Variation in ϕ and ω directions is not that clear although an increasing tendency in peak widths is still evident. Therefore, we can conclude that increased BZO content modifies the in-plane growth of YBCO, increasing the width of XRD peak in ϕ-direction, and thus leading to increased number of low-angle grain boundaries [48–50], as well as weakened lattice ordering along the YBCO c-direction as broadened ω peaks demonstrate. However, since the similar tendency is not that clear in the microstrain ε_{WH} calculated from the Williamson–Hall analysis [51], we can conclude that the effect of non-coherent domain size somehow compensates the nonuniform microstrain in the YBCO lattice. As can be seen in Table 1, the intensity ratio $I(005)/I(004)$ does not significantly vary, being well below 20, indicating that all the films regardless of BZO doping concentration are well-oxygenated [52].

Evolution of the YBCO microstructure and growth of the BZO nanorods with increasing dopant concentrations were investigated by HRTEM, and the most important results are shown in the TEM images of Fig. 2 and collected in Table 2. As evident from the TEM images, all measured BZO concentrations exhibit intrinsic structural defects, including stacking faults, alongside BZO nanorods oriented approximately along the out-of-plane direction of the films. However, the size, number, and distribution of these defects vary significantly depending on the BZO dopant concentration.

As depicted in Table 2, the diameter of the nanorods undergoes an insignificant change, and the tilting angle of the rods remains nearly constant as the BZO concentration increases. However, as anticipated, the average distances between nanorods decrease significantly with an increase in the BZO concentration, leading to a greater number of nanorods within the film. Moreover, the average length of nanorods experiences a substantial decrease with an increasing BZO concentration. In sample 4BZO, the nanorods' length is approximately half the thickness of the entire film, while in sample 12BZO, it reduces to only a quarter of the film's thickness. These alterations in both the number and length of nanorods hold great significance for flux pinning.

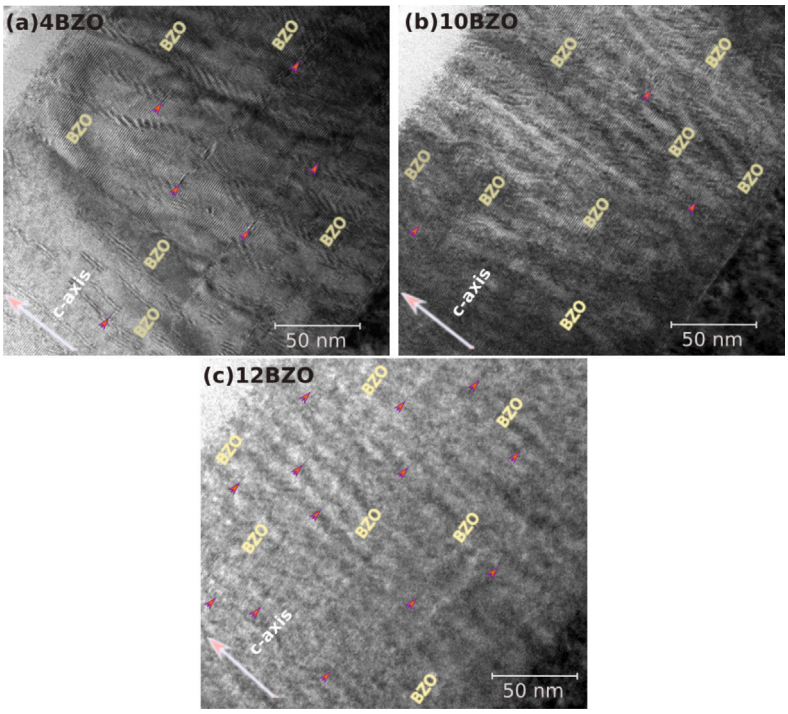

Fig. 2. Cross-sectional HR-TEM images of samples 4BZO, 10BZO, and 12BZO are presented. The metallic substrate's top buffer layer is visible in the bottom right corner, while the film surface can be observed in the upper left corner. The BZO nanorods are clearly visible in all samples, although their lengths and distributions differ significantly, as indicated in Table 2. Additionally, the lengths of the stacking faults along the *ab*-plane, denoted by pink arrows, exhibit significant variations depending on the concentration of BZO doping.

Table 2
A collection of the most important TEM results related to the film thickness, the length and distribution of the stacking faults (SF) as well as the critical parameters of the BZO nanorods such as their average diameter (d), length (l), spacing (s) and tilting angle (t).

Sample	Film thickness (nm)	SF length (nm)	SF	d (nm)	l (nm)	s (nm)	t (°)
4BZO	220 ± 10	35/12	Bottom half	6.3 ± 0.6	98 ± 20	20.5 ± 3.5	9 ± 5
10BZO	195 ± 5	7.5	Only a few	5.8 ± 0.7	85 ± 20	6.3 ± 1.5	10 ± 6
12BZO	215 ± 5	8.5	Great number	5.7 ± 0.8	55 ± 15	5.7 ± 1.8	9 ± 6

Changes in the lengths of nanorods, *i.e.* nanorod fragmentation, may be related to the length of the stacking faults, but particularly to their number. The systematic study on the size and distribution of stacking faults was performed using cross-sectional TEM, with the findings summarized in Table 2. In sample 4BZO, stacking faults are primarily concentrated in the lower layers of the film, resulting in longer average lengths along the *ab*-plane direction, approximately 35 nm. Conversely, on the surface layer of sample 4BZO, only a few stacking faults are present, and even those that exist are notably shorter, measuring around 12 nm. Sample 10BZO exhibits an average stacking fault length of approximately 7.5 nm, but their overall count is quite low. In contrast, the number of stacking faults significantly increases in sample 12BZO, which likely contributes to the limited growth of BZO nanorods. The results clearly show that the stacking fault density is influenced by strain relaxation and accommodation resulting from the complex interaction between the crystal lattice, strain, and self-assembled APCs [53]. An 8% lattice mismatch between YBCO and BZO leads to 1D nanocolumnar defects [54,55], with optimal strain at 10% BZO, which minimizes the number of stacking faults. Higher BZO content increases strain and defect density due to excessive APC formation. This aligns with our XRD results and previous studies [37], indicating that 10% BZO doping is optimal for reducing defects and maintaining nanorod alignment along the *c*-axis.

Table 3
Superconducting properties determined from the ac susceptibilities, resistivity measurements and magnetic hysteresis loops measured at 10 K.

Sample	$T_{c,mag}$ (K)	$\Delta T_{c,mag}$ (K)	$T_{c,res}$ (K)	$J_{c,0\ T,10\ K}$ (MA/cm^2)	$B^*_{10\ K}$ (mT)
0BZO	87.9	1.1	91.6	60.8	95
2BZO	84.9	3.6	89.9	35.6	323
4BZO	83.1	2.7	89.6	35.9	453
6BZO	80.5	3.7	89.6	21.6	305
8BZO	76.9	4.1	89.6	10.1	235
10BZO	71.0	5.7	88.8	5.2	104
12BZO	65.2	7.5	88.1	3.4	67

3.2. Superconducting properties with increased BZO concentration

From the ac susceptibility measurements, we have defined superconducting critical temperatures $T_{c,mag}$s and transition widths for all the YBCO films doped with different BZO concentrations. As can be seen in Table 3, onset $T_{c,mag}$ decreases linearly with increasing BZO concentration, having values of ≈88 K for undoped YBCO, ≈83 K and ≈65 K for 4BZO and 12BZO, respectively. The transition widths $\Delta T_{c,mag}$s, defined by the temperature difference between 10% and 90% points of the full transition curve, increase almost linearly with increasing BZO content, from barely 1 K for undoped YBCO up to just over 7 K in 12BZO film. These results are well in line with our XRD results, where increased amount of disordering decreases $T_{c,mag}$ and broadens

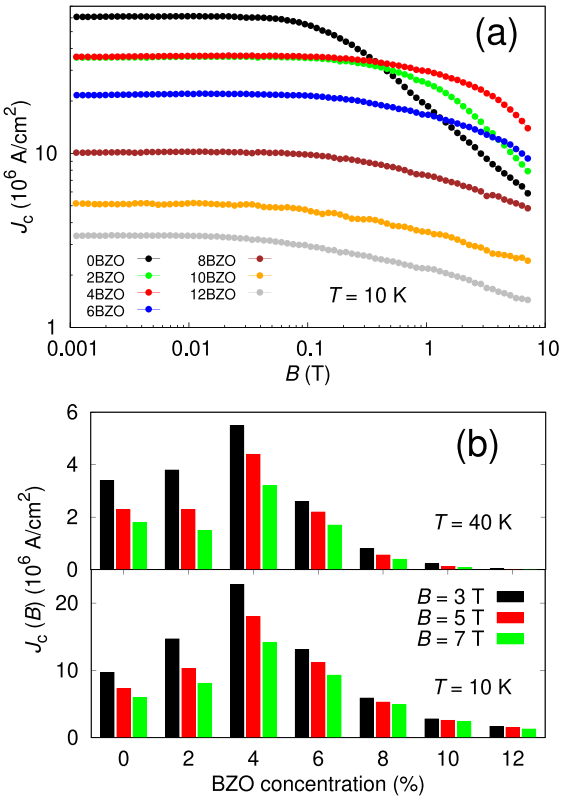

Fig. 3. The magnetic field dependences of J_cs determined from the opening of the magnetic hysteresis loops measured at 10 K for the differently BZO-doped YBCO films deposited on buffered metallic templates (a). (b) shows the relative in-field (3, 5 and 7 T) $J_c(B)$s measured at temperatures 10 K and 40 K when compared with the $J_c(0)$ values.

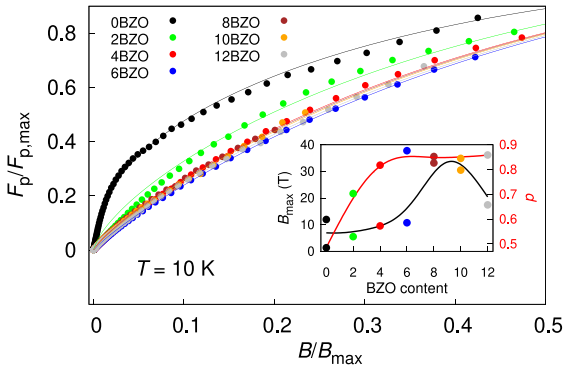

Fig. 4. The magnetic field dependent pinning force data fitted to Eq. (1) for all the YBCO films doped with different BZO concentrations. The inset shows how the actual flux pinning related exponent p and the magnetic field value B_{max}, where F_p reaches its maximum, depends on the number of the BZO nanorods.

the superconducting transition. However, upon comparing the $T_{c,mag}$ values with the resistively measured $T_{c,res}$, it becomes evident that in relatively thin small-scale samples, the optimal current path leads to significantly increased T_c in resistivity measurements [11,56].

When concentrating on the field dependent $J_c(B)$ curves determined from the magnetic hysteresis loops carried out at 10 K and 40 K, we have obtained that the self-field $J_c(0)$, i.e. J_c at 0 T and 10 K, decreases significantly with increasing BZO concentration, as can be seen in Table 3 and Fig. 3. In addition, the low-field plateau, where J_c decreases only marginally and single vortex pinning dominates, reaches the maximum value of $B^* = 453$ mT in 4BZO film. With higher BZO concentration, B^* starts to decrease linearly, indicating that the nanorod fragmentation can modify the vortex distribution and their mutual interaction even at smaller magnetic fields [57,58]. As can be seen in Fig. 3(a) and (b), the in-field $J_c(B)$ and thus the flux pinning properties are remarkably changed with increasing BZO concentration. Although the absolute $J_c(B)$ is highest in 4BZO film among all the BZO doped YBCO films in whole magnetic field range, the relative improvement in $J_c(B)$ when compared with the $J_c(0)$ at 10 depends on the magnetic field range. Particularly, the highest improvement in J_c below BZO concentration ≲4% is obtained at ≈3 T, while at higher BZO concentrations, the relatively highest J_c occurs at higher fields. Instead at 40 K, the relative improvement in J_c is always maximal around 3 T, regardless of the BZO doping concentration.

To study the effect of actual flux pinning, by extracting the effect of $J_c(0)$ which always has an important role in absolute $J_c(B)$ value, we have precisely investigated the shapes of the $J_c(B)$ curves above B^*. First, we have determined the scaled pinning force function $F_p/F_{p,max}$ by using the formula $F_p(B) = BJ_c(B)$, which allows us to express the formula in its simplified form [59–61]

$$\frac{F_p(B)}{F_{p,max}} = \frac{(p+q)^{p-1}p^q}{q^q}\left(\frac{B}{B_{max}}\right)^p\left(\frac{p+q}{p} - \frac{B}{B_{max}}\right)^q, \quad (1)$$

where we have only two free parameters p and q related to the size and number of the pinning centers together with their impact on vortex lattice (Fig. 4). The parameter q is obtained being very close to value 1.1 [61] and thus we have collected the most important flux pinning related parameters in the inset of Fig. 4. Here, the field B_{max}, where the fitted F_p function reaches its maximum value well beyond the measurement range (main panel of Fig. 4), has a maximum of approximately 30 T around a BZO concentration of 8%–10%, which clearly corresponds to the highest number of BZO nanorods. In addition, the flux pinning related exponent p reaches its maximum of ≈0.85 around BZO content of 4% and it stays roughly the same up to the highest dopant concentration of 12%. Interpreting these results together, we can draw the conclusion that for the flux pinning alone, it would be optimal to choose a BZO dopant concentration of 8%–10% for the applications, where the YBCO thin films have been grown on a buffered metallic substrate. This BZO content is also consistent with the previously attained level of 10% for YBCO films on single crystal STO substrates, which has been found to maximize pinning when the distance between the outer edge of the nanorods is on the order of the diameter of the nanorod [37].

3.3. Angular dependent critical current densities

In the in-field angular dependent $J_c(\theta)$ analysis (Fig. 5), we have limited the measurements on the most relevant BZO doping concentrations, since the main focus has been in finding the maximal BZO content that can be used in different magnetic field ranges. In general, we can conclude that the absolute J_c values (not shown here) decrease with increasing BZO doping concentration, which is obviously related to the reduction of the effective volume of the superconducting YBCO and shortened electron mean free path, since the lattice periodicity is disturbed by the BZO dopant induced defects [24]. Moreover, one remarkable feature is that J_c is always largest in the direction of the *ab*-plane. This can be seen in all samples regardless of the BZO concentration and external magnetic field. However, the broadening of the *ab*-peak is also substantial with increasing BZO content. These issues can be explained by the YBCO intrinsic pinning by the CuO_2 planes as well as the BZO induced relatively short and randomly distributed stacking faults, as also observed earlier at high fields [34].

Since we are more interested in flux pinning and not the absolute value of J_c, we focus on comparing the shapes of the $J_c(\theta)$ curves and the formation of the *c*-peak, as shown in Fig. 5. At lower BZO doping

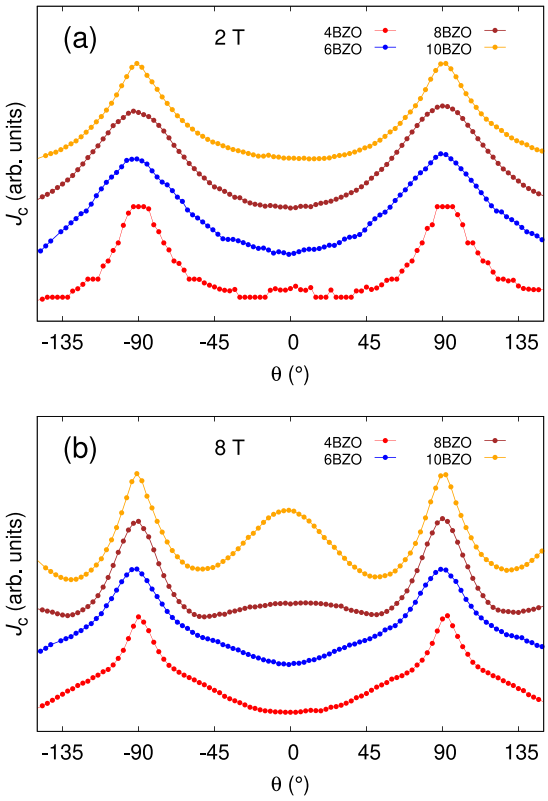

Fig. 5. The angle dependent critical current densities J_c measured under 2 T (a) and 8 T (b) fields at 40 K for YBCO films doped with different BZO concentrations. The angles $\theta = 0°$ and $\theta = \pm 90°$ correspond the YBCO c-axis and ab-plane, respectively. The $J_c(\theta)$ curves have been shifted in the y-direction to compare the detailed shapes of the curves.

concentrations of 4 and 6%, there appears to be c-axis pinning in the 2 T measurements, as the J_c level in the vicinity of 0° is larger than in the 8 T measurements. In 2 T, the BZO nanorods pin the small number of vortices in the c-axis direction, but in 8 T, the BZO rods are too few compared to the number of vortices, causing bending of the vortices, which in turn widens the ab-peak observed in $J_c(\theta)$ [15,19,62,63]. At high BZO concentrations of 8 and 10% in a high magnetic field of 8 T, a clear peak in the c-axis direction is formed in the $J_c(\theta)$ curve, which clearly indicates a growing collective pinning along the c-axis as the number of vortices increases [35,63,64]. This is in good agreement with the previously presented TEM results, where the number of BZO nanorods oriented along the c-axis in the YBCO lattice is at a maximum at a BZO concentration of 10%. At BZO concentration of 12% (not shown here), the critical current is dramatically decreased, and the ab-peak in the $J_c(\theta)$ curve exhibits significant broadening, while the c-axis peak is entirely absent [63]. This observation aligns with the findings from the TEM measurements, which clearly indicate a higher concentration of stacking faults and thus fragmented BZO nanorods within the film [34,62].

3.4. Mechanism behind maximized flux pinning

We have earlier concluded that, in BZO-doped YBCO films grown on single crystalline $SrTiO_3$ substrate, the vortex pinning performance and consequently the J_c is fundamentally limited by the density of the nanorod lattice [37]. For the BZO nanorods on STO substrate, closely mimicking an idealized situation, the critical limit is set by nanorod density at which the nanorod average spacing equals to their diameter. Increasing the nanorod lattice density above this point degrades the hopping potential energy barrier between adjacent nanorods, making the thermally activated flow of vortices (hopping) increasingly more pronounced. Here, however, the fragility of the metallic substrate degrades the coherent structure of the BZO nanorods making the conclusion about the critical density of the nanorod lattice [37] invalid for the samples studied herein. In particular, the effects of stacking fault induced nanorod fragmentation should not be ignored [37]. In order to investigate the effect of BZO concentration (nanorod spacing) along with the observed nanorod fragmentation, we have considered a simple 1-dimensional pinning model only considering nanorod and vortices both oriented parallel to YBCO c-axis. The pinning potential associated with a single nanorod of radius R centered at $x = x'$ has been addressed using the formula [65]

$$u_0(x, x') = \epsilon_0 \cdot \frac{R^2}{2 \cdot (x - x')^2 + 4\xi^2}, \tag{2}$$

where ϵ_0 is pinning energy coefficient and $\xi \approx 1.5$ nm is the low-temperature superconducting coherence length for YBCO. It is important to note that ϵ_0 scales with the length of the nanorod. That is, the depth of the pinning potential for a single piece of f-times fragmented nanorod would be ϵ_0/f. If the fragments would be perfectly aligned on top of each other, their total pinning potential would equal to ϵ_0. Otherwise, both the depth and the shape of $\epsilon(x)$ would be altered with respect to an ideal nanorod penetrating through the whole film.

We have studied this effect by the overall pinning energy landscape given by

$$E(x) = \sum_{f=1}^{f} \sum_{i=1}^{N} \frac{u_0(x' = x_{i-1} + \Delta x + U(-2R, 2R))}{f}, \tag{3}$$

where f equals to the number of nanorod fragments, $\Delta x = (x_N - x_0)/(N-1)$, in which N represents the total number of nanorods (unrelated to f), and the function $U(a, b)$ represents a function that returns uniformly distributed random numbers between a and b. Looking at the TEM images in Fig. 2, we have allowed the center of a fragmented nanorod to shift a maximum distance of $2R$, so that in the extreme case the edges of the fragments would line up. The considered fragmentation of the nanorod is schematically illustrated in Fig. 6(a), while examples of the resulting pinning potentials for solid and fragmented nanorods are shown in Fig. 6(b). The fragmentation clearly has a striking effect on the periodicity of the pinning potential.

Next, we aim to relate the nanorods average edge-to-edge spacing (s) and fragmentation (f) to the experimental observations presented in the inset of Fig. 4. The experimentally measured B_{max} is defined as the field where the maximum value of the F_p is reached. Since the $F_p(B)$ represents the overall pinning force within the sample, its value increases with the number of sufficiently pinned vortices ($\sim B$). The decrease of $F_p(B)$ will be observed after a new induced vortex cannot locate a sufficiently strong pinning center to get trapped. Instead, the vortex–vortex interactions start to perturb the pinning of the previously pinned vortices and $F_p(B)$ consequently decreases. The value of B_{max} is thus proportional to the number (density) of the effective pinning sites. While increasing the field naturally affects the overall pinning potential landscape via more prominent vortex–vortex interactions, B_{max} is ultimately limited by the number of effective potential wells under zero field. By effective pinning centers we refer to potential wells whose depth exceeds a given limit. While this limit is evidently temperature dependent, here it can be considered completely arbitrary, since we are not considering the temperature dependence nor the absolute values of B_{max} and the corresponding experiments were conducted at a fixed low-temperature limit (Fig. 4).

Based on the above discussion, we have numerically calculated the average number of potential wells ($\sim B_{max}$) with depth smaller than $\epsilon_0/2$ resulting from Eq. (3). The calculations were performed in a 1-dimensional grid comparable to a size of 1000 nm ($x_0 = -500$ nm, $x_N = 500$ nm) using a total of $2 \cdot 10^4$ points corresponding to a resolution of 0.05 nm. The number of nanorods positioned within

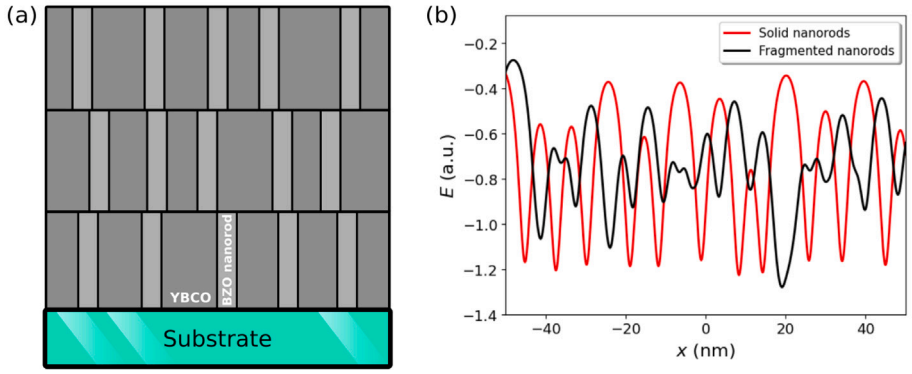

Fig. 6. (a) A schematic illustration of the considered fragmentation (here $f = 3$) of the nanorod lattice. (b) An example of the calculated pinning potentials (Eq. (3)) for 1-dimensional array of solid ($f = 1$) and fragmented (here $f = 3$) nanorods.

the grid evidently determines the average s. The positions ((x, E)-coordinates) of the local energy minima and maxima were determined as the points where the derivative of the $E(x)$ curve changes from negative to positive (minimum) and vice versa (maximum). The depth of the potential well was then determined as the difference between two adjacent energy minimum and maximum. Note, that only one of the maximums surrounding a potential well was used to determine the energy difference since the direction of vortex motion would in any case be biased by the applied current. This enables the efficient calculation of the number of effective pinning potentials as the average of five statistical repetitions. As an example, the overall shapes of the studied pinning potentials resulting from Eq. (3) are illustrated in Fig. 6(b).

Fig. 7(a) presents the calculated normalized B_{max} as a function of average nanorod separation for different fragmentations. Vice versa, Fig. 7(b) presents B_{max} as a function of fragmentation for different nanorod separations. These results give a clear picture about the combined effect of s and f. Firstly, for small fragmentations $f \leq 2$, B_{max} decreases as a function of s. This is evident, as the increasing s is equivalent of decreasing the density of the nanorod lattice. It is interesting to observe that this effect gets diminished for high nanorod fragmentations $f \geq 3$. In fact for $f = 5$, B_{max} can be observed to slightly increase with s. This happens because the fragmentation of the nanorods disturbs the periodicity of the pinning potential particularly for small nanorod separations, manifesting as the presence of large number of shallow ineffective pinning potentials giving rise to more prominent thermal vortex creep. Fig. 7(b) demonstrates how efficiently the nanorod fragmentation degrades the number of efficient pinning centers. One can observe that increasing f from 1 (no fragmentation) to 2 results in significant decrease of B_{max} observed for all nanorod spacings, although for small values of s this is clearly more prominent. For $f \geq 2$, B_{max} corresponding to all s decrease monotonically in a similar fashion. Clearly the fragmentation affects B_{max} already at very small extent.

The above presented results could explain the experimentally observed behavior of the pinning parameter p and B_{max} as a function of BZO content ($\sim s$) presented in the inset of Fig. 4. The observed increasing B_{max} as a function of BZO content up to 10% would then suggest that below this dopant concentration the nanorod fragmentation is negligible. The observed decrease in B_{max} for 12% BZO would result from the stacking fault induced nanorod fragmentation supported by the TEM results (Table 2). At the same time, the pinning parameter p does not show signs of degradation as a function of BZO content since effective pinning centers are still present despite the fragmentations, only their number is reduced. These observations are in line with the above theoretical model. In conclusion, the presence of stacking faults results in increased nanorod fragmentation, which degrades the value of B_{max}, and consequently J_c under large fields.

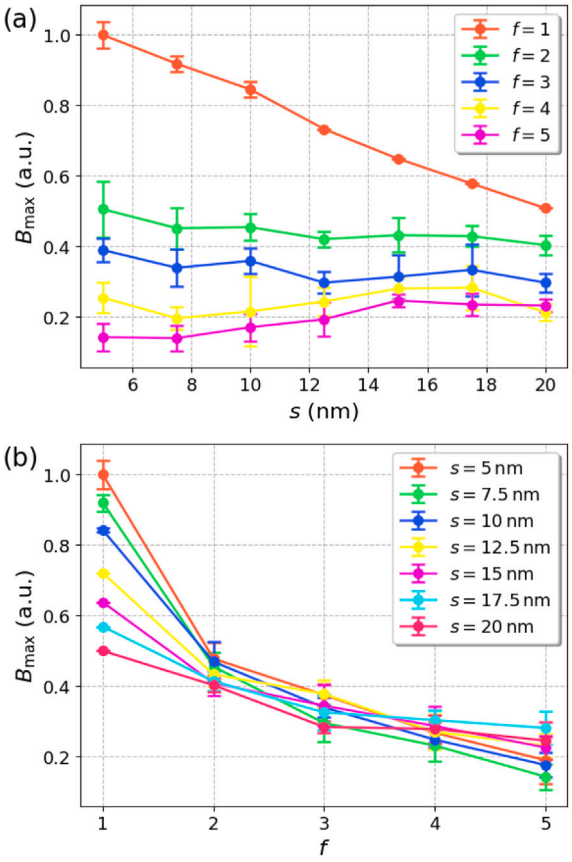

Fig. 7. B_{max} as a function of (a) average nanorod separation (s) for different fragmentations (f) and (b) as a function of nanorod fragmentation for different average separations. B_{max} has been considered proportional to the number (density) of effective pinning potential $u(x)$ resulting from Eq. (3) for which $\min(u(x)) < \epsilon_0/2$.

4. Conclusions

In conclusion, our comprehensive investigation into the influence of BZO nanorod density on magnetic flux pinning in YBCO thin films has provided significant insights. Through detailed structural analysis, we have identified distinct alterations in grain boundaries and nanorod distribution with varying BZO concentrations. Notably, the superconducting properties, including critical current density, have exhibited a discernible dependence on BZO concentration, particularly in high magnetic fields. Our findings highlight an optimal BZO doping level

of 8%–10% for maximizing flux pinning in YBCO films on buffered metallic substrates. Furthermore, the emergence of a *c*-axis peak in the angular dependent critical current curves at elevated BZO concentrations underscores the importance of collective pinning mechanisms. The quantitative discussion on the effects of nanorod spacing and fragmentation complemented our experimental observations, offering deeper insights into the underlying mechanisms driving the observed enhancements in flux pinning. Overall, our study contributes significantly to advancing the understanding and optimization of YBCO thin films for high-field applications, laying the groundwork for the development of high-performance coated conductor layer structures.

CRediT authorship contribution statement

T. Vaimala: Writing – original draft, Methodology, Investigation, Formal analysis, Conceptualization. **M.M. Aye:** Writing – original draft, Methodology, Investigation, Formal analysis. **E. Rivasto:** Writing – original draft, Software, Methodology, Formal analysis. **Y. Zhao:** Writing – review & editing, Resources. **H. Huhtinen:** Writing – review & editing, Visualization, Validation, Supervision, Methodology, Formal analysis, Conceptualization. **P. Paturi:** Writing – review & editing, Supervision, Project administration, Funding acquisition, Conceptualization.

Declaration of competing interest

The authors declare the following financial interests/personal relationships which may be considered as potential competing interests: Hannu Huhtinen reports financial support was provided by Jenny and Antti Wihuri Foundation. If there are other authors, they declare that they have no known competing financial interests or personal relationships that could have appeared to influence the work reported in this paper.

Data availability

Data will be made available on request.

Acknowledgments

The Jenny and Antti Wihuri Foundation, Finland is acknowledged for financial support and the Finnish IT Center for Science (CSC) and the FGCI project (Finland) for the computational resources.

References

[1] S.R. Foltyn, L. Civale, J.L. MacManus-Driscoll, Q.X. Jia, B. Maiorov, H. Wang, M. Maley, Materials science challenges for high-temperature superconducting wire, Nature Mater. 6 (2007) 631–642.

[2] T.G. Holesinger, L. Civale, B. Maiorov, D.M. Feldmann, J.Y. Coulter, D.J. Miller, V.A. Maroni, Z. Chen, D.C. Larbalestier, R. Feenstra, X. Li, Y. Huang, T. Kodenkandath, W. Zhang, M.W. Rupich, A.P. Malozemoff, Progress in nanoengineered microstructures for tunable high-current, high-temperature superconducting wires, Adv. Mater. 20 (2008) 391–407.

[3] X. Obradors, T. Puig, Coated conductors for power applications: materials challenges, Supercond. Sci. Technol. 27 (2014) 044003, 1–17.

[4] S.M. Anlage, Microwave superconductivity, IEEE J. Microw. 1 (2021) 389–402.

[5] J. Golm, S. Arguedas Cuendis, S. Calatroni, C. Cogollos, B. Döbrich, J. Gallego, J. García Barceló, X. Granados, J. Gutierrez, I. Irastorza, T. Koettig, N. Lamas, J. Liberadzka-Porret, C. Malbrunot, W. Millar, P. Navarro, C. Carlos, T. Puig, G. Rosaz, M. Siodlaczek, G. Telles, W. Wuensch, Thin film (high temperature) superconducting radiofrequency cavities for the search of axion dark matter, IEEE Trans. Appl. Supercond. 32 (2022) 1500605, 1–5.

[6] D. Larbalestier, A. Gurevich, D.M. Feldmann, A. Polyanskii, High-T_c superconducting materials for electric power applications, Nature 414 (2001) 368–377.

[7] S. Kang, A. Goyal, J. Li, A.A. Gapud, P.M. Martin, L. Heatherly, J.R. Thompson, D.K. Christen, F.A. List, M. Paranthaman, D.F. Lee, High performance high-T_c superconducting wires, Science 311 (2006) 1911–1914.

[8] C.V. Varanasi, J. Burke, L. Brunke, H. Wang, M. Sumption, P.N. Barnes, Enhancement and angular dependence of transport critical current density in pulsed laser deposited $YBa_2Cu_3O_{7-x}$+$BaSnO_3$ films in applied magnetic fields, J. Appl. Phys. 102 (2007) 063909, 1–5.

[9] S.H. Wee, A. Goyal, Y.L. Zuev, C. Cantoni, High performance superconducting wire in high applied magnetic fields via nanoscale defect engineering, Supercond. Sci. Technol. 21 (2008) 092001, 1–4.

[10] A.C. Wulff, A.B. Abrahamsen, A. Insinga, Topical review: Multifilamentary coated conductors for ultra-high magnetic field applications, Supercond. Sci. Technol. 34 (2021) 053003, 1–29.

[11] M.Z. Khan, E. Rivasto, H. Rijckaert, Y. Zhao, M.O. Liedke, M. Butterling, A. Wagner, I. Van Driessche, H. Huhtinen, P. Paturi, Strongly enhanced growth of high-temperature superconducting films on an advanced metallic template, Cryst. Growth Des. 22 (2022) 2097–2104.

[12] W.H. Fietz, R. Heller, S.I. Schlachter, W. Goldacker, Application of high temperature superconductors for fusion, Fusion Eng. Des. 86 (2011) 1365–1368.

[13] P. Bruzzone, W.H. Fietz, J.V. Minervini, M. Novikov, N. Yanagi, Y. Zhai, J. Zheng, High temperature superconductors for fusion magnets, Nucl. Fusion 58 (2018) 103001, 1–13.

[14] G. Blatter, V.B. Geshkenbein, A.I. Larkin, From isotropic to anisotropic superconductors: A scaling approach, Phys. Rev. Lett. 68 (1992) 875–878.

[15] G. Blatter, M. Feigel'man, V. Geshkenbein, A. Larkin, V. Vinokur, Vortices in high-temperature superconductors, Rev. Modern Phys. 66 (1994) 1125–1388.

[16] N.J. Long, N.M. Strickland, E.F. Talantsev, Modeling of vortex paths in HTS, IEEE Trans. Appl. Supercond. 17 (2007) 3684–3687.

[17] L. Civale, B. Maiorov, A. Serquis, J.O. Willis, J.Y. Coulter, H. Wang, Q.X. Jia, P.N. Arendt, J.L. MacManus-Driscoll, M.P. Maley, S.R. Foltyn, Angular-dependent vortex pinning mechanisms in $YBa_2Cu_3O_7$ coated conductors and thin films, Appl. Phys. Lett. 84 (2004) 2121–2123.

[18] L. Civale, B. Maiorov, A. Serquis, S.R. Foltyn, Q.X. Jia, P.N. Arendt, H. Wang, J.O. Willis, J.Y. Coulter, T.G. Holesinger, J.L. MacManus-Driscoll, M.W. Rupich, W. Zhang, X. Li, Influence of crystalline texture on vortex pinning near the *ab*-plane in $YBa_2Cu_3O_7$ thin films and coated conductors, Physica C 412–414 (2004) 976–982.

[19] P. Paturi, The vortex path model and angular dependence of J_c in thin YBCO films deposited from undoped and $BaZrO_3$-doped targets, Supercond. Sci. Technol. 23 (2010) 025030, 1–7.

[20] L. Civale, B. Maiorov, J.L. MacManus-Driscoll, H. Wang, T.G. Holesinger, S.R. Foltyn, A. Serquis, P.N. Arendt, Identification of intrinsic ab-plane pinning in $YBa_2Cu_3O_7$ thin films and coated conductors, IEEE Trans. Appl. Supercond. 15 (2005) 2808–2811.

[21] T. Puig, J. Gutiérrez, A. Pomar, A. Llordés, J. Gázquez, S. Ricart, F. Sandiumenge, X. Obradors, Vortex pinning in chemical solution nanostructured YBCO films, Supercond. Sci. Technol. 21 (2008) 034008, 1–12.

[22] P. Paturi, M. Malmivirta, T. Hynninen, H. Huhtinen, Angle dependent molecular dynamics simulation of flux pinning in YBCO superconductors with artificial pinning sites, J. Phys.: Condens. Matter. 30 (2018) 315902, 1–7.

[23] A. Stangl, A. Palau, G. Deutscher, X. Obradors, T. Puig, Ultra-high critical current densities of superconducting $YBa_2Cu_3O_{7-\delta}$ thin films in the overdoped state, Sci. Rep. 11 (2021) 8176, 1–12.

[24] P. Paturi, H. Huhtinen, Roles of electron mean free path and flux pinning in optimizing the critical current in YBCO superconductors, Supercond. Sci. Technol. 35 (2022) 065007, 1–9.

[25] E. Rivasto, T. Hynninen, H. Huhtinen, P. Paturi, Optimization of high-temperature superconducting bilayer structures using a vortex dynamics simulation, J. Phys.: Condens. Matter. 35 (2023) 075701, 1–10.

[26] S.R. Foltyn, L. Civale, J.L. MacManus-Driscoll, Q.X. Jia, B. Maiorov, H. Wang, M. Maley, Materials for sustainable energy: A collection of peer-reviewed research and review articles from nature publishing group, 2011, pp. 299–310.

[27] M.K. T. J. Haugan, J. Wu, Artificial pinning centers in (Y, RE)-Ba-Cu-O superconductors: Recent progress and future perspective, Supercond. Sci. Technol. 33 (2019) 040301, 1–5.

[28] J. MacManus-Driscoll, S. Wimbush, Processing and application of high-temperature superconducting coated conductors, Nat. Rev. Mater. 6 (2021) 587, 1–18.

[29] K. Tsuchiya, X. Wang, S. Fujita, A. Ichinose, K. Yamada, A. Terashima, A. Kikuchi, Superconducting properties of commercial REBCO-coated conductors with artificial pinning centers, Supercond. Sci. Technol. 34 (2021) 105005, 1–13.

[30] J. Zhang, H. Wu, G. Zhao, L. Han, J. Zhang, Progress in the study of vortex pinning centers in high-temperature superconducting films, Nanomaterials 12 (2022) 4000, 1–23.

[31] J.L. MacManus-Driscoll, S.R. Foltyn, Q.X. Jia, H. Wang, A. Serquis, L. Civale, B. Maiorov, M.E. Hawley, M.P. Maley, D.E. Peterson, Strongly enhanced current densities in superconducting coated conductors of $YBa_2Cu_3O_{7-x}$+$BaZrO_3$, Nature Mater. 3 (2004) 439–443.

[32] A. Goyal, S. Kang, K.J. Leonard, P.M. Martin, A.A. Gapud, M. Varela, M. Paranthaman, A.O. Ijadoula, E.D. Specht, J.R. Thompson, D.K. Christen, S.J. Pennycook, F.A. List, Irradiation. free, Columnar defects comprised of self-assembled nanodots and nanorods resulting in strongly enhanced flux pinning in $YBa_2Cu_3O_{7-\delta}$ films, Supercond. Sci. Technol. 18 (2005) 1533–1538.

[33] B. Maiorov, S.A. Baily, H. Zhou, O. Ugurlu, J.A. Kennison, P.C. Dowden, T.G. Holesinger, S.R. Foltyn, L. Civale, Synergetic combination of different types of defect to optimize pinning landscape using $BaZrO_3$-doped $YBa_2Cu_3O_7$, Nature Mater. 8 (2009) 398–404.
[34] M.Z. Khan, E. Rivasto, J. Tikkanen, H. Rijckaert, M. Malmivirta, M.O. Liedke, M. Butterling, A. Wagner, H. Huhtinen, I. Van Driessche, P. Paturi, Enhanced flux pinning isotropy by tuned nanosized defect network in superconducting $YBa_2Cu_3O_{6+x}$ films, Sci. Rep. 9 (2019) 15425, 1–12.
[35] E. Rivasto, M.Z. Khan, M. Malmivirta, H. Rijckaert, M.M. Aye, T. Hynninen, H. Huhtinen, I.V. Driessche, P. Paturi, Self-assembled nanorods in YBCO matrix – a computational study of their effects on critical current anisotropy, Sci. Rep. 10 (2020) 3169, 1–14.
[36] E. Rivasto, M.Z. Khan, Y. Wu, Y. Zhao, C. Chen, J. Zhu, H. Huhtinen, P. Paturi, Lattice defect induced nanorod growth in YBCO films deposited on an advanced IBAD-MgO template, Supercond. Sci. Technol. 33 (2020) 075008, 1–8.
[37] M.M. Aye, E. Rivasto, H. Rijckaert, H. Palonen, H. Huhtinen, I. Van Driessche, P. Paturi, Optimized $BaZrO_3$ nanorod density in $YBa_2Cu_3O_{6+x}$ matrix for high field applications, Supercond. Sci. Technol. 35 (2022) 075006, 1–10.
[38] M.M. Aye, E. Rivasto, T. Vaimala, Y. Zhao, H. Huhtinen, P. Paturi, Improved crystalline quality and self-field j_c in sequentially vacuum-multilayered YBCO thin films on buffered metallic templates, IEEE Trans. Appl. Supercond. 33 (2023) 6601806, 1–6.
[39] E. Rivasto, M. Todorovic, H. Huhtinen, P. Paturi, Optimization of high-temperature superconducting multilayer films using artificial intelligence, New J. Phys. 25 (2023) 113046, 1–15.
[40] E. Rivasto, M.M. Aye, H. Huhtinen, P. Paturi, Enhanced critical current density in optimized high-temperature superconducting bilayer thin films, J. Phys.: Condens. Matter. 36 (2024) 135702, 1–9.
[41] A. Goyal, D.F. Lee, F.A. List, E.D. Specht, R. Feenstra, M. Paranthaman, X. Cui, S.W. Lu, P.M. Martin, D.M. Kroeger, D.K. Christen, B.W. Kang, D.P. Norton, C. Park, D.T. Verebelyi, J.R. Thompson, R.K. Williams, T. Aytug, C. Cantoni, Recent progress in the fabrication of high-J_c tapes by epitaxial deposition of YBCO on RABiTS, Physica C 357–360 (2001) 903.
[42] Y. Iijima, K. Kakimoto, M. Kimura, K. Takeda, T. Saitoh, Reel to reel continous formation of Y-123 coated conductors by IBAD and PLD method, IEEE Trans. Appl. Supercond. 11 (2001) 2816.
[43] Y. Zhao, L. Ma, W. Wu, H.-L. Suo, J.-C. Grivel, Study on advanced $Ce_{0.9}La_{0.1}O_2/Gd_2Zr_2O_7$ buffer layers architecture towards all chemical solution processed coated conductors, J. Mater. Chem. A 3 (2015) 13275–13282.
[44] Y. Zhao, J.-M. Zhu, G.-Y. Jiang, C.-S. Chen, W. Wu, Z.-W. Zhang, S.K. Chen, Y.M. Hong, Z.-Y. Hong, Z.-J. Jin, Progress in fabrication of second generation high temperature superconducting tape at Shanghai Superconductor Technology, Supercond. Sci. Technol. 32 (2019) 044004.
[45] H. Palonen, H. Huhtinen, M.A. Shakhov, P. Paturi, Electron mass anisotropy of $BaZrO_3$ doped YBCO thin films in pulsed magnetic fields up to 30 T, Supercond. Sci. Technol. 26 (2013) 045003, 1–5.
[46] M.M. Aye, E. Rivasto, M.Z. Khan, H. Rijckaert, E. Salojärvi, C. Haalisto, E. Mäkilä, H. Palonen, H. Huhtinen, I. Van Driessche, P. Paturi, Control of the nanosized defect network in superconducting thin films by target grain size, Sci. Rep. 11 (2021) 6010, 1–11.
[47] H.P. Wiesinger, F.M. Sauerzopf, H.W. Weber, On the calculation of J_c from magnetization measurements on superconductors, Physica C 203 (1992) 121–128.
[48] R. Kromann, J.B. Bilde-Sørensen, R. de Reus, N.H. Andersen, P. Vase, T. Freltoft, Relation between critical current densities and epitaxy of YBCO thin films on MgO and $SrTiO_3$, J. Appl. Phys. 71 (1992) 3419–3426.
[49] P. Paturi, M. Peurla, K. Nilsson, J. Raittila, Crystalline orientation and twin formation in YBCO thin films laser ablated from a nanocrystalline target, Supercond. Sci. Technol. 17 (2004) 564–570.
[50] P. Paturi, M. Peurla, J. Raittila, N.H. Andersen, Dependence of critical current density on crystalline direction in thin YBCO films, Physica C 433 (2005) 123–131.
[51] M. Birkholz, Thin Film Analysis by X-Ray Scattering, Wiley-VCH, 2006.
[52] J. Ye, K. Nakamura, Quantitative structure analyses of YBCO thin films: Determination of oxygen content from x-ray-diffraction patterns, Phys. Rev. B 48 (1993) 7554–7564.
[53] T. Horide, F. Kametani, S. Yoshioka, T. Kitamura, K. Matsumoto, Structural evolution induced by interfacial lattice mismatch in self-organized $YBa_2Cu_3O_{7-\delta}$ nanocomposite film, ACS Nano 11 (2017) 1780–1788.
[54] J. Wu, J. Shi, J. Baca, R. Emergo, A. Elliot, J. Wilt, M.A. Sebastian, T. Haugan, C.V. Varanasi, Probing microscopic strain interplay due to impurity doping and vicinal growth and its effect on pinning landscape in YBCO films, IEEE Trans. Appl. Supercond. 25 (2015) 8000205, 1–5.
[55] J. Wu, J. Shi, Interactive modeling-synthesis-characterization approach towards controllable in situ self-assembly of artificial pinning centers in RE-123 films, Supercond. Sci. Technol. 30 (2017) 103002, 1–15.
[56] A.V. Pan, I.A. Golovchansky, S.A. Fedoseev, Critical current density: Measurement vs. reality, EPL 103 (2013) 17006.
[57] F.C. Klaassen, G. Doornbos, J.M. Huijbregtse, R.C.F. van der Geest, B. Dam, R. Griessen, Vortex pinning by natural linear defects in thin films of $YBa_2Cu_3O_{7-\delta}$, Phys. Rev. B 64 (2001) 184523, 1–20.
[58] L. Krusin-Elbaum, L. Civale, J.R. Thompson, C. Feild, Accommodation of vortices to columnar defects: Evidence for large entropic reduction of vortex localization, Phys. Rev. B 53 (1996) 11744–11750.
[59] M.J. Qin, Z.X. Shi, H.L. Ji, X. Ji, X.X. Yao, H.C. Li, X.S. Rong, Paramagnetism and scaling behavior of volume flux pinning force density in a $GdBa_2Cu_30_{6+x}$ thin films, J. Appl. Phys. 78 (1995) 3287–3292.
[60] C.V. Varanasi, P.N. Barnes, J. Burke, Enhanced flux pinning force and uniquely shaped flux pinning force plots observed in $YBa_2Cu_3O_{7-x}$ films with $BaSnO_3$ nanoparticles, Supercond. Sci. Technol. 20 (2007) 1071–1075.
[61] P. Paturi, M. Malmivirta, H. Palonen, H. Huhtinen, Dopant diameter dependence of $j_c(B)$ in doped YBCO films, IEEE Trans. Appl. Supercond. 26 (2016) 8000705, 1–5.
[62] N.J. Long, Model for the angular dependence of critical currents in technical superconductors, Supercond. Sci. Technol. 21 (2008) 025007, 1–8.
[63] S. Wimbush, N. Long, The interpretation of the field angle dependence of the critical current in defect-engineered superconductors, New J. Phys. 14 (2012) 083017, 1–24.
[64] M.M. Aye, E. Rivasto, M.Z. Khan, H. Rijckaert, H. Palonen, H. Huhtinen, I. Van Driessche, P. Paturi, Multilayering BZO nanocolumns with different defect densities for YBCO high field applications, New J. Phys. 23 (2021) 113031, 1–12.
[65] G. Blatter, M.V. Feigel'man, V.B. Geshkenbein, A.I. Larkin, V.M. Vinokur, Vortices in high-temperature superconductors, Rev. Modern Phys. 66 (1994) 1125–1388.